PROTEINS
STRUCTURE ■ FUNCTION ■ BIOINFORMATICS

Toward elucidating the heat activation mechanism of the TRPV1 channel gating by molecular dynamics simulation

Han Wen,[1] Feng Qin,[2] and Wenjun Zheng[1]*

[1] Department of Physics, State University of New York at Buffalo, Buffalo, New York 14260

[2] Department of Physiology and Biophysical Sciences, State University of New York at Buffalo, Buffalo, New York 14260

ABSTRACT

As a key cellular sensor, the TRPV1 cation channel undergoes a gating transition from a closed state to an open state in response to various physical and chemical stimuli including noxious heat. Despite years of study, the heat activation mechanism of TRPV1 gating remains enigmatic at the molecular level. Toward elucidating the structural and energetic basis of TRPV1 gating, we have performed molecular dynamics (MD) simulations (with cumulative simulation time of 3 μs), starting from the high-resolution closed and open structures of TRPV1 solved by cryo-electron microscopy. In the closed-state simulations at 30°C, we observed a stably closed channel constricted at the lower gate (near residue I679), while the upper gate (near residues G643 and M644) is dynamic and undergoes flickery opening/closing. In the open-state simulations at 60°C, we found higher conformational variation consistent with a large entropy increase required for the heat activation, and both the lower and upper gates are dynamic with transient opening/closing. Through ensemble-based structural analyses of the closed state versus the open state, we revealed pronounced closed-to-open conformational changes involving the membrane proximal domain (MPD) linker, the outer pore, and the TRP helix, which are accompanied by breaking/forming of a network of closed/open-state specific hydrogen bonds. By comparing the closed-state simulations at 30°C and 60°C, we observed heat-activated conformational changes in the MPD linker, the outer pore, and the TRP helix that resemble the closed-to-open conformational changes, along with partial formation of the open-state specific hydrogen bonds. Some of the residues involved in the above key hydrogen bonds were validated by previous mutational studies. Taken together, our MD simulations have offered rich structural and dynamic details beyond the static structures of TRPV1, and promising targets for future mutagenesis and functional studies of the TRPV1 channel.

Proteins 2016; 84:1938–1949.

Key words: average structure; gating; heat activation; hydrogen bonds; membrane proximal domain; molecular dynamics; principal component analysis; root mean square fluctuation; TRPV1 channel.

INTRODUCTION

The transient receptor potential (TRP) channels are a superfamily of cation channels,[1,2] which can be activated by various physical and chemical stimuli such as heat,[3,4] cold,[5–7] voltage,[8] acid,[9,10] force,[11–13] and exogenous ligands (e.g., capsaicin[4]). The TRP channels make promising drug targets[14,15] because of their involvements in various signaling pathways linked to diseases.[16,17] As a prototype TRP channel, TRPV1 forms a homo-tetramer, with each subunit comprised of a six-helix (S1–S6) transmembrane domain (TMD) and an intracellular domain (ICD) [see Fig. 1(a)]. Similar to the voltage-gated ion channels,[18,19] the TMD of TRPV1 consists of two structural domains—the S1–S4 domain on the channel periphery and the S5–S6 pore domain enclosing a central pore [see Fig. 1(a)]. Unlike the voltage-gated ion channels, the TRP channels lack a charged S4 helix although their gating has a weak voltage dependence.[20] The N-terminal portion of ICD forms an ankyrin repeats domain (ARD).[21] The C-terminal domain (CTD) of

Additional Supporting Information may be found in the online version of this article.

Grant sponsor: American Heart Association; Grant number: #14GRNT18980033 (W.Z.); Grant sponsor: National Science Foundation; Grant number: #0952736 (W.Z.); Grant sponsor: National Institutes of Health; Grant number: #GM104521 (F.Q.).

*Correspondence to: Wenjun Zheng, 239 Fronczak Hall, Buffalo, NY 14260. E-mail: wjzheng@buffalo.edu

Received 30 June 2016; Revised 3 September 2016; Accepted 24 September 2016
Published online 3 October 2016 in Wiley Online Library (wileyonlinelibrary.com). DOI: 10.1002/prot.25177

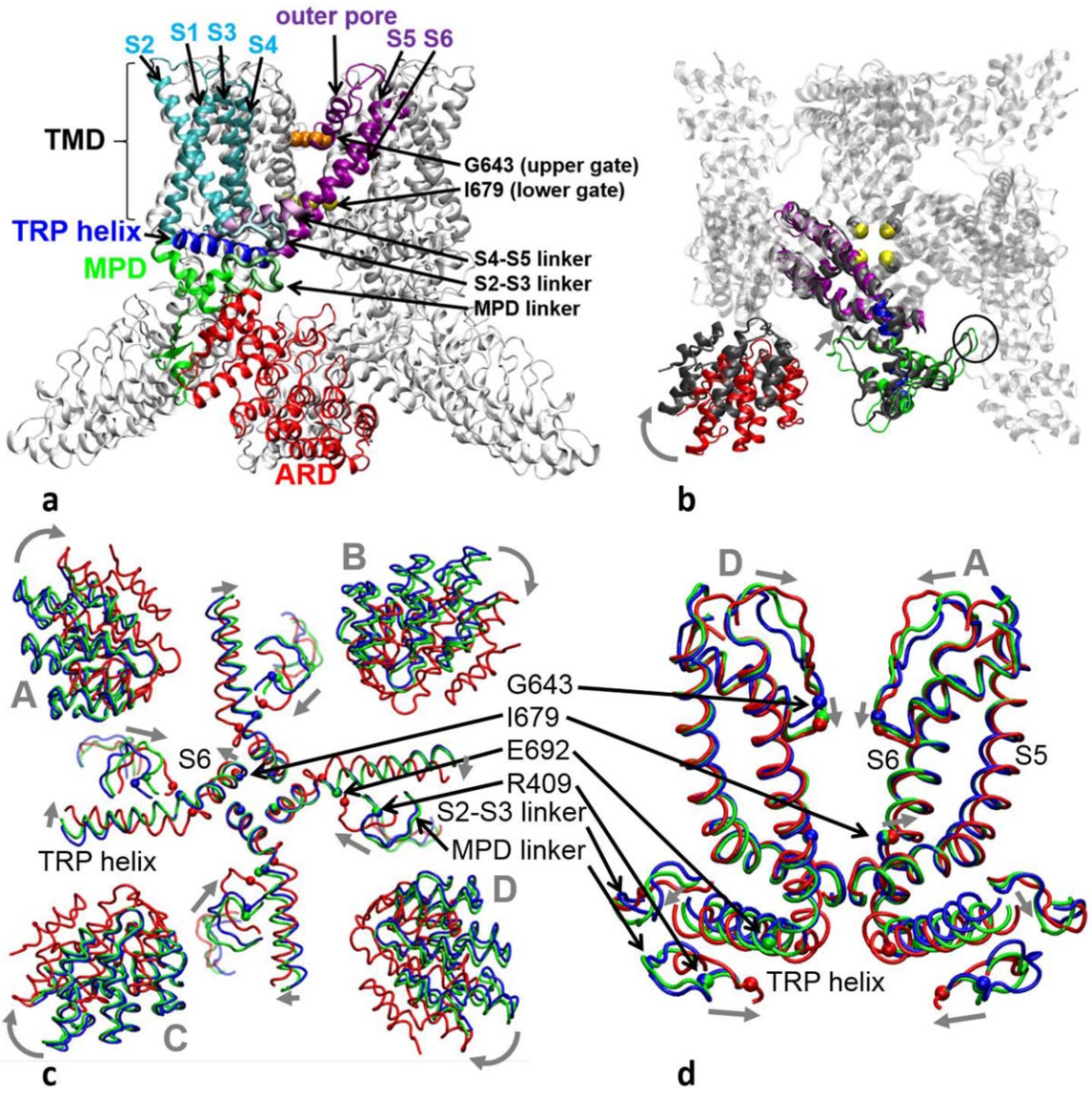

Figure 1

Structural architecture and changes in TRPV1: (**a**) side view of TRPV1 structure: the following color scheme is used for a representative subunit—the ARD (red), the MPD (green), the MPD linker (light green), the S1–S4 helices (cyan), the S2–S3 linker (light cyan), the S4–S5 linker (light purple), the pore domain (purple, including the outer pore, the S5 helix, and the S6 helix), and the TRP helix (blue). The remaining subunits are colored in silver. Residues G643 and I679 at the upper and the lower gate are shown as spheres colored in orange and yellow, respectively. (**b**) Bottom view of TRPV1 structure: a representative subunit of the closed TRPV1 structure is colored with the same color coding as (a) (part of the ARD and the S1-S4 helices are omitted for clarity), while the rest is in silver. A subunit of the open TRPV1 structure is superimposed in the pore domain and colored in gray. A clockwise rotation of the ARD, an inward motion of the MPD linker, and an outward motion of I679 are shown by arrows. The inter-subunit contacts between the ARD and the MPD are circled. (**c**) and (**d**) show the average structures of the C-state (blue), the heated-C-state (green), and the O-state (red) ensembles in the bottom view and the side view, respectively. These average structures are superimposed in the pore domain. In (c), only part of the ARDs, the MPD linkers, the S2–S3 linkers, the lower S6 helices, and the TRP helices are shown with key motions marked by gray arrows. In (d), only the MPD linkers, the S2–S3 linkers, the pore domain, and the TRP helices are shown in two diagonally opposing subunits, with key motions marked by gray arrows. Residues R409, E692, G643, and I679 (as markers for the MPD linker, the TRP helix, the upper gate, and the lower gate, respectively) are shown as spheres. Four subunits of the TRPV1 tetramer (A, B, C, and D) are labeled.

ICD contains a stretch of highly conserved residues forming an alpha helix known as the TRP helix,[22] which has been implicated in the coupling of stimulus sensing to the TRPV1 gating[23] and interactions with other proteins and ligands.[24,25] At the TMD–ICD interface is a membrane proximal domain [MPD, including linker residues 400–415, see Fig. 1(a)], which was found to contribute to heat activation in the TRPV subfamily.[26]

Alternative heat-activation sites were proposed within the CTD,[27–29] the outer pore, and the pore domain.[30–33] The specific functions of these sites in heat activation remain unclear as to whether they mediate temperature sensing or other gating events downstream of temperature sensing such as allosteric coupling.[34] The above functional domains are connected by several flexible linkers, including the S2–S3 linker involved in vanilloid binding,[35] and the S4–S5 linker which is thought to push/pull the S6 helix to open the channel gate in voltage-gated ion channels[36] and TRPV1.[35]

Structural studies by cryo-electron microscopy (cryo-EM) resulted in low-resolution (>13 Å) structures of several TRP channels.[37–43] X-ray crystallography was also used to determine high-resolution structures for various fragments of the TRP channels, including the ARD of the TRPV channels.[44–50] But high-resolution structures of full-length TRP channels remained unavailable until recently. In 2013, the labs of Julius and Cheng used cryo-EM to determine the structures of a minimal functional construct of the rat TRPV1 in three distinct forms at 3–4 Å resolutions[35,51]—a closed apo structure, an open structure bound with double-knot toxin (DkTx, a peptide toxin) and resiniferatoxin (RTX, a vanilloid agonist), and a partially open structure bound with capsaicin (a vanilloid agonist). These structures revealed a dual-gate channel pore with two constrictions [see Fig. 1(a)]—an upper gate (selectivity filter) near the outer pore (residues G643 and M644) and a lower gate in the lower S6 helix (residue I679). Both gates are closed (open) in the closed (open) structure, while the upper gate is closed and the lower gate is partially open in the capsaicin-bound structure.[35,51] These and other subsequently solved high-resolution structures[52–54] have paved the way for quantitative structure-driven studies of the TRP-channel gating mechanism. However, because these structures were solved at very low temperature, they do not offer direct insights to the heat activation mechanism.

Molecular dynamics (MD) simulation is the method of choice for investigating protein dynamics and energetics under physiological conditions with atomic details,[55] which has been applied to various ion channels.[56–59] However, MD simulation is highly expensive, demanding the use of a massively parallelized or special-purpose supercomputer (such as Anton[59]). Thanks to recent developments in computing hardware and software (such as the use of graphics processing units to accelerate MD simulation[60]), one can now routinely simulate a large biomolecular system (with $\geq 10^5$ atoms) at a speed of 1–10 ns/day on a single computer node. However, it remains challenging for MD to access the μs–ms time scales relevant to many biomolecular transitions (including the gating transition in TRPV1). Among various strategies to overcome the time-scale limit of MD simulation, coarse-grained modeling (e.g., the elastic network model[61–63]) has been developed using reduced protein representations and simplified force fields.[64,65]

In a recent study,[66] we performed a combined coarse-grained modeling and all-atom MD simulation starting from the new TRPV1 structures.[35,51] Our normal mode analysis captured two key modes of collective motions involved in the TRPV1 gating transition, featuring a global twist motion of the ICD relative to the TMD as observed between the closed and open structure [see Fig. 1(b)]. Our transition pathway modeling predicted a sequence of structural movements that propagate from the ARD to the TMD via the MPDs and the CTDs, leading to an eventual opening of the channel pore. Additionally, our MD simulation of the ICD fragment identified key residues in the MPD and the CTD that contribute differently to the nonpolar energy of the open and closed state, and these residues were predicted to control the temperature sensitivity of TRPV1 gating.

In this study, we have conducted MD simulations of the TRPV1 tetramer in the closed (C) and the open (O) state at 30°C and 60°C, respectively. Our goal is to probe the structural and dynamic changes between the C-state and the O-state ensembles underlying the thermodynamics of TRPV1 gating. To further probe heat-activated conformational changes, we have performed additional MD simulations at 60°C starting from the closed structure.

MATERIALS AND METHODS

MD simulation setup

We downloaded pre-oriented PDB files of the closed (PDB id: 3j5p) and the open structure (PDB id: 3j5q) of TRPV1 from the OPM database.[67] We used the MODLOOP webserver[68] to model the missing residues 503–507 of the S2–S3 linker. We used the Membrane Builder function[69–71] of the CHARMM-GUI webserver[72,73] to embed TRPV1 in a bilayer of 1-palmitoyl-2-oleoyl phosphatidylcholine (POPC) lipids surrounded by a box of water and ions (with 15-Å buffer of water/lipids extending from the protein in each direction). The closed-state (open-state) system contains total 261,443 (252,560) atoms, including 53,589 (51,972) water molecules and 464 (434) POPC molecules. To ensure 0.15*M* ionic concentration and zero net charge, 170 (164) K^+ and 194 (188) Cl^- ions were added in the closed-state (open-state) system. To maintain the key inter-subunit contacts between each ARD and the MPD of an adjacent subunit [see Fig. 1(b)], we added inter-subunit harmonic restraints between the Cα atoms of residue pairs 376–245 and 375–210 with a spring constant of 500 kJ/mol/nm^2. After energy minimization, six steps of equilibration were performed (with gradually reduced harmonic restraints applied to protein, lipids, water, and ions). Finally we conducted production MD runs in the NPT ensemble. The Nose–Hoover method[74] was used

with temperature $T = 30$°C or 60°C. The Parrinello–Rahman method[75] was used for pressure coupling. A 10-Å switching distance and a 12-Å cutoff distance were used for nonbonded interactions. The particle mesh Ewald method[76] was used for electrostatics calculations. The LINCS algorithm[77] was used to constrain the hydrogen-containing bond lengths, which allowed a 2-fs time step for MD simulation. The energy minimization and MD simulation were performed with the GROMACS program[78] version 5.0.3 using the CHARMM36 force field[79,80] and TIP3P water model.[81]

Root mean square fluctuation analysis

To quantify the flexibility of TRPV1 at individual residue positions during our MD simulations, we calculated the root mean square fluctuation (RMSF) as follows: first, we saved 1500 snapshots from all 200-ns MD trajectories of the C state at 30°C, the heated C state at 60°C, or the O state at 60°C (with the first 50 ns of each trajectory discarded) to build a structural ensemble; second, we superimposed the Cα coordinates of residues 400–710 onto the initial structure with a minimal root mean square deviation (RMSD); finally, we calculated the following RMSF at residue position n: $RMSF_n = \sqrt{(1/M)\sum_{m=1}^{M} |\vec{r}_{mn} - \langle \vec{r}_n \rangle|^2}$, where $\vec{r}_{mn}$ is the Cα position of residue n in snapshot m, $\langle \vec{r}_n \rangle = (1/M)\sum_{m=1}^{M} \vec{r}_{mn}$ is the average Cα position of residue n, and $M = 1500$ is the total number of snapshots. We calculated the average of $RMSF_n$ for four equivalent residue positions n of the TRPV1 tetramer. We assessed the overall flexibility of TRPV1 using the following root mean square average of RMSF over residues 400–710: $\langle RMSF \rangle = \sqrt{(1/N)\sum_{n=400}^{710} RMSF_n^2}$, where $N = 288$ is the number of residues between 400 and 710.

PCA analysis

To identify dominant modes of motions involved in the TRPV1 gating, we performed the principal component analysis (PCA) as follows: first, we combined the C-state and O-state ensembles; second, we superimposed the Cα coordinates of each snapshot onto the initial structure 3j5p with a minimal RMSD; third, we calculated a co-variance matrix comprised of the following 3 × 3 block matrices $C_{nn'} = (1/M)\sum_{m=1}^{M} (\vec{r}_{mn} - \langle \vec{r}_n \rangle) \otimes (\vec{r}_{mn'} - \langle \vec{r}_{n'} \rangle)$ (see above for definitions of symbols); fourth, we diagonalized the co-variance matrix and kept top two PCA modes (denoted PC1 and PC2) with the highest eigenvalues.

Hydrogen bond analysis

We used the following geometric criteria to identify a hydrogen bond (HB) between two polar non-hydrogen atoms (i.e., acceptor and donor): the donor–acceptor distance is <3.5 Å, and the deviation of the donor–hydrogen–acceptor angle from 180° is <60°. We used the VMD program[82] to identify and calculate the occupancy of each HB within a structural ensemble. For each HB-forming residue pair, we calculated its occupancy by summing up the occupancy of HBs between them for all four subunits and then dividing it by 4. We only considered those HB-forming residue pairs with occupancy ≥0.3.

RESULTS

Equilibrium MD simulations of TRPV1 in the C state and the O state

To explore the conformational dynamics of TRPV1 in the C state, we conducted five 200-ns MD simulations at 30°C (with different initial random seeds), starting from a system of a closed TRPV1 structure (PDB id: 3j5p) surrounded by a lipid bilayer and a box of water and ions (see Materials and Methods section). The TRPV1 channel is known to be stably closed at 30°C according to previous studies.[4,83] The five MD trajectories were combined to form a structural ensemble of the C state (excluding the beginning 50 ns when the initial structure undergoes relaxation and equilibration, see Supporting Information Fig. S1). Then we performed various analyses for this combined structural ensemble (see below). The goal of this simulation is to elucidate the equilibrium dynamics of TRPV1 in the C state (see below).

To further explore the O-state ensemble of TRPV1, we conducted five 200-ns MD simulations at 60°C, starting from the open structure of TRPV1 (PDB id: 3j5q). The TRPV1 channel is activated by heat and stably open at 60°C.[4,83] Therefore, we did not include DkTx and RTX to stabilize the open channel in our simulations. We have ensured that TRPV1 is adequately relaxed and equilibrated after the removal of these ligands within 50 ns of the simulations (see Supporting Information Fig. S1). The five MD trajectories were combined to form a structural ensemble of the O state (excluding the beginning 50 ns). This simulation aims to characterize the equilibrium dynamics of TRPV1 in the O state in comparison with the C state (see below).

In an attempt to simulate the heat activation of TRPV1, we conducted five 200-ns MD simulations at 60°C, starting from the closed structure, which were then combined to generate a structural ensemble of the heated C state. Although 60°C is high enough to thermally activate the TRPV1 gating,[83] we did not observe channel opening owning to limited simulation time. Nevertheless, we did observe significant structural and dynamic changes in TRPV1 evoked by heat activation (see below).

TRPV1 exhibits greater conformational variation in the O state than in the C state

To assess the conformational stability of TRPV1 in simulation, we calculated the root mean square deviation

(RMSD) of Cα atoms relative to the initial structure for each of the three ensembles (for the C state, the O state, and the heated C state, respectively). Overall, the TRPV1 tetramer shows relatively high RMSD in the C state at 30°C (5.0 ± 0.9 Å, see Supporting Information Fig. S1) and the heated C state at 60°C (5.5 ± 1.0 Å), and even higher RMSD in the O state at 60°C (7.6 ± 1.5 Å, see Supporting Information Fig. S1). This could be attributed to the lack of extensive contacts between the ICDs of neighboring subunits [see Fig. 1(b)],[35] and may be an inherent feature of the TRPV1 channel known to possess high entropy (particularly in the O state).[83] We note that this large RMSD is unlikely caused by missing residues in the CTD because our preliminary simulation of the new closed TRPV1 structure[52] (with the missing CTD residues added) still show similarly high RMSD (data not shown).

We then calculated RMSD for the core TRPV1 structure [denoted the expanded TMD, including residues 400–710 comprising the MPD linker, the TMD, and the TRP helix, see Fig. 1(a)]. It shows relatively low RMSD in the C state at 30°C (2.3 ± 0.2 Å, see Supporting Information Fig. S1), the heated C state at 60°C (2.5 ± 0.2 Å), and the O state at 60°C (3.2 ± 0.3 Å, see Supporting Information Fig. S1), which is comparable to previous MD simulations based on high-resolution X-ray structures of voltage-gated channels (with RMSD = 3–4 Å).[84–86] This supports the stability of our TRPV1 simulations despite using cryo-EM structures with only 3–4 Å resolutions.

To further explore the conformational variation in the C state and the O state, we calculated all-to-all RMSD for the expanded TMD in each of the three ensembles. In the C state at 30°C, the distribution of all-to-all RMSD peaks at 2.8 Å (see Supporting Information Fig. S2). In the O state at 60°C, the distribution peaks at 3.8 Å (see Supporting Information Fig. S2). Therefore, the O-state ensemble is conformationally more diverse than the C-state ensemble, which is consistent with a higher entropy in the O state than in the C state[83] as required for the heat activation of TRPV1 gating. For the heated C-state ensemble at 60°C, the distribution of all-to-all RMSD also peaks at 2.8 Å (see Supporting Information Fig. S2) with a minor peak at 3.2 Å. So it is intermediate between the C-state and the O-state distributions, suggesting that heat may increase the conformational diversity of the C-state ensemble. This increase cannot be attributed to an unspecific thermal effect caused by higher temperature (see below).

The O state shows greater flexibility than the C state in specific heat-sensitive regions

To assess the conformational flexibility at individual residue positions in the expanded TMD, we calculated the RMSF in each of the three ensembles (see Materials and Methods). For the C-state ensemble at 30°C, the

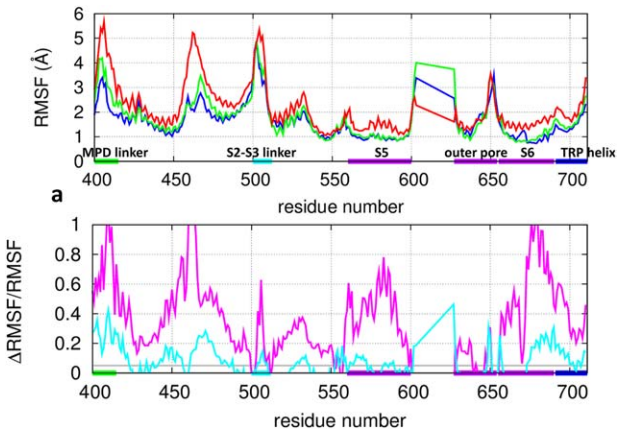

Figure 2

Results of RMSF analysis for TRPV1: (**a**) RMSF at individual residue positions in the expanded TMD (blue: the C state at 30°C, green: the heated C state at 60°C, red: the O state at 60°C). (**b**) The fractional RMSF changes (purple: from the C state to the O state, cyan: from the C state to the heated C state). The average $RMSF_n$ for four equivalent residue positions n of the TRPV1 tetramer is shown. The residue positions corresponding to the MPD linker, the S2–S3 linker, the S5 and S6 helices, the outer pore, and the TRP helix are marked by horizontal bars [same color coding as Fig. 1(a)].

RMSF profile exhibits pronounced peaks at E405 of the MPD linker, N467 of the S1-S2 linker, S502 of the S2-S3 linker, K603 and N652 of the outer pore, and the C terminus of the TRP helix [see Fig. 2(a)]. For the O-state ensemble at 60°C, the RMSF profile shows higher peaks in the above regions [see Fig. 2(a)]. The above flexible regions are known to be functionally important (e.g., the MPD linker in heat activation,[26] the S2–S3 linker in capsaicin binding,[87] the outer pore in proton regulation[9,88] and heat activation,[30–33] and the TRP helix in allosteric coupling[23]). Our finding of a flexible outer pore supports the notion that TRPV1 features a structurally dynamic outer pore critical to the TRPV1 activity.[9,33,88–90]

To further assess the RMSF differences between the C and the O state, we calculated the fractional change in RMSF from the C state to the O state [denoted ΔRMSF/RMSF, see Fig. 2(b)]. For control, a temperature increase from 30 to 60°C would increase RMSF by $\sqrt{333/303}-1 \approx 5\%$ due to an unspecific thermal effect. So we deem a C-to-O RMSF difference to be significant if ΔRMSF/RMSF > 5%. Using the above criterion, we found pronounced RMSF increases in the MPD linker, the S1–S2 linker, the S2–S3 linker, the S5 helix, the S6 helix, and the TRP helix [see Fig. 2(b)]. Overall, the O state at 60°C has higher RMSF ($\langle RMSF \rangle_O = 1.70$ Å) than the C state at 30°C ($\langle RMSF \rangle_C = 1.25$ Å), which is much higher than 5% as expected for an unspecific thermal effect. This RMSF increase is due to more diverse conformations sampled in the O state, which is consistent with the finding of larger all-to-all RMSD in the O state (see Supporting Information Fig. S2).

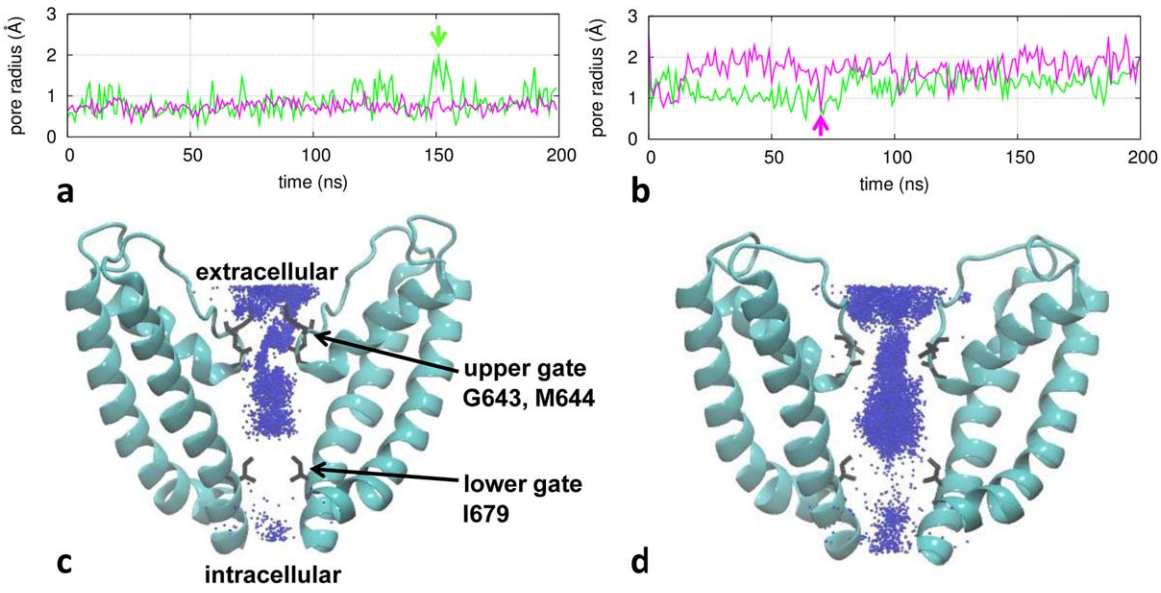

Figure 3

Results of channel pore analysis for TRPV1: (**a**) pore radius at the upper gate (green) and the lower gate (purple) as a function of time for a representative trajectory in the C state at 30°C; (**b**) pore radius for a representative trajectory in the O state at 60°C; (**c**) a density map of K^+ ions for the C-state ensemble; (**d**) a density map of K^+ ions for the O-state ensemble. In (a) and (b), two snapshots with transient upper gate opening and lower gate closing are marked by vertical arrows. In (c) and (d), two diagonally opposing subunits are shown with gate residues G643, M644, and I679 labeled, and K^+ ions are depicted as blue points. [Color figure can be viewed at wileyonlinelibrary.com]

To probe the effect of heat on flexibility, we compared RMSF between the C-state ensembles of 30°C and 60°C. As shown by the ΔRMSF/RMSF profile, the most pronounced increases are in the MPD linker, the S1–S2 linker, the outer pore, and the lower S6 helix [see Fig. 2(b)], which partially overlap with the regions of large C-to-O RMSF differences [see Fig. 2(b)]. This encouraging finding suggests that the above heat-sensitive regions (particularly the MPD linker[26] and the outer pore[30–33]) may be involved in the heat activation of TRPV1 gating.

A back-of-the-envelope estimation of the C-to-O entropy change for the expanded TMD (total 4 × 288 residues) gave $\Delta S \sim k_B \ln(\langle \mathrm{RMSF} \rangle_O / \langle \mathrm{RMSF} \rangle_C) \times 4 \times 288 \sim 500$ cal/mol/K, where $\langle \mathrm{RMSF} \rangle_O = 1.70$ Å at 60°C and $\langle \mathrm{RMSF} \rangle_C = 1.35$ Å at 60°C. This estimation is comparable to the large entropy change (310 cal/mol/K) from a previous electrophysiology study,[83] supporting the relevance of our MD simulations to the gating thermodynamics of TRPV1.

Channel pore analysis reveals a dynamic upper gate in the C state and dynamic upper/lower gates in the O state

To assess the open/closed state of the TRPV1 channel pore and quantify its dynamics during the MD simulations, we used the HOLE program[91] to calculate the pore radius along the pore axis for snapshots of each of the three ensembles. We focused on the pore radius at the upper gate and the lower gate (defined as the minimal pore radius of the upper and lower half of the channel pore, respectively). Based on the pore radius calculations for 5 × 150 snapshots from each of the three ensembles, we estimated the probability of the upper/lower gate being water permeable (i.e., with radius >1.15 Å) with a maximal standard error of $\sqrt{0.5^2/750} = \sim 1.8\%$.

In the C state at 30°C, the pore radius at the lower gate is 0.75 ± 0.14 Å [see Fig. 3(a)] with 0% of snapshots being water permeable, suggesting the lower gate is stably closed and impermeable to water/ions. The minimal-radius position of the lower gate is predominantly at I679 in 96% of snapshots, supporting the proposed role of I679 as the lower gate[35] instead of Y671 identified by a previous cysteine accessibility measurement.[92] At the upper gate, the pore radius is 0.83 ± 0.31 Å [see Fig. 3(a)] with 15% of snapshots being water permeable, which indicates a more dynamic upper gate than the lower gate featuring transient opening [see Fig. 3(a)]. The minimal-radius position of the upper gate fluctuates between G643 (in 54% of snapshots) and M644 (in 34% of snapshots).

In the heated C state at 60°C, the pore radius at the lower gate is 0.81 ± 0.16 Å with 3% of snapshots being water permeable. At the upper gate, the pore radius is 0.91 ± 0.30 Å with 16% of snapshots being water permeable. Therefore, heat only slightly opens the lower and upper gates while the channel remains largely impermeable to water/ions within the 200-ns simulation time.

In the O state at 60°C, the pore radius at the lower gate is 1.75 ± 0.43 Å [see Fig. 3(b)], and 90% of snapshots are water permeable, suggesting the lower gate is more open than in the C state. At the upper gate, the pore radius is 1.25 ± 0.32 Å [see Fig. 3(b)], and 51% of snapshots are water permeable. Therefore, while the lower gate is more open than the upper gate on average, both gates are fairly dynamic with large fluctuations in pore radius indicative of transient opening/closing [see Fig. 3(b)]. This elevated lower gate dynamics is consistent with our finding of large RMSF increase in the lower S6 helix from the C state to the O state [see Fig. 2(b)]. Such dynamic behaviors of the lower/upper gates may be related to the experimental observations that the opening of TRPV1 involves flickery openings/closings that occur in bursts[10,93,94] despite differences in time scale between simulations and experiments.

We further plotted a density map of K^+ ions within the channel pore as sampled by our simulations (at a rate of 0.25 ns per frame) in the C state and the O state [see Fig. 3(c,d)]. In the C state at 30°C, we observed K^+ ions distributing continuously (discontinuously) through the upper (lower) gate, suggesting a non-conducting channel constricted at the lower gate [see Fig. 3(c)]. In contrast, in the O state at 60°C, the entire channel pore is accessible to K^+ ions, which is consistent with a conducting channel [see Fig. 3(d)]. Indeed, we observed three K^+ permeation events in two 200-ns MD trajectories of the O state at 60°C (see Supporting Information Fig. S3).

State-dependent conformational changes in the outer pore, the MPD linker, and the TRP helix are involved in heat activation of TRPV1 gating

To explore conformational changes involved in heat-activated TRPV1 gating, we calculated the average structures for the C-state, heated-C-state, and O-state ensembles, and superimposed them along the TMD [see Fig. 1(c,d)]. Unlike the symmetric cryo-EM structures, the ensemble-averaged structures of the TRPV1 tetramer undergo asymmetric changes in the four subunits [labeled A–D, see Fig. 1(c,d)] between the above states. We have verified that the observed changes between the average structures are robust and insensitive to how the ensembles are constructed (e.g., using different segments/subsets of the MD trajectories).

At the lower gate, the I679 square opens asymmetrically in the O state relative to the C state [with RMSD = 1.3 Å, more open in subunit A/B than in subunit C/D, see Fig. 1(c)]. The I679 square in the heated C state is essentially as closed as in the C state (with RMSD = 0.2 Å) except in subunit A where I679 is intermediate between the C state and the O state [see Fig. 1(c)].

At the upper gate, residues G643 move vertically (i.e., parallel to the channel axis) downward from the C state to the O state [with RMSD = 2.1 Å, see Fig. 1(d)], which are accompanied by inward motions of the outer pore region [with RMSD = 2.3 Å, see Fig. 1(d)]. Interestingly, G643 and other outer pore residues adopt intermediate positions in the heated C state [with RMSD = 1.3 Å, see Fig. 1(d)].

Outside the channel pore, we observed large structural changes from the C state to the O state in the ARDs, the MPD linkers, the S2–S3 linkers, and the TRP helices [with RMSD = 7.1, 5.0, 3.1, and 3.3 Å, respectively, see Fig. 1(c,d)], while the S4–S5 linkers undergo little change (with RMSD = 1.1 Å). The ARDs undergo a ~9° clockwise rotation as observed in cryo-EM.[35,51,54] The MPD linkers move inward to engage with the TRP helices that bend at their junctions with the adjoined S6 helices. The S2–S3 linkers undergo more complex motions distinct from the MPD linkers. Interestingly, similar yet smaller changes were observed from the C state to the heated C state in the ARDs, the MPD linkers, and the TRP helices of some subunits [with RMSD = 0.9, 2.0, and 1.3 Å, respectively, see Fig. 1(c,d)].

Among the above C-to-O conformational changes, the coupled motions of the MPD linkers and the TRP helices suggest a possible heat-activation pathway from the heat-sensing MPD[26] to the TRP helix and subsequently to the lower gate. Instead of pulling the TRP helix (and the adjoined lower S6 helix) outward to open the lower gate, these motions cause a narrowing of the channel on the intra-cellular side [see Fig. 1(d)], which is in contrast to the widening of the channel at the lower gate. Additionally, on the extra-cellular side of the channel, the outer pore also shows a narrowing from the C state to the O state [see Fig. 1(d)]. Therefore, the gating of TRPV1 seems to involve simultaneous narrowing and widening in different parts of the channel pore. In agreement with our finding, similar inward motions on the intra-cellular and extra-cellular sides of the channel were observed in past FRET studies of gating in TRPV1[31] and potassium channel.[95]

PCA reveals heat-activated and gating-related changes in structural ensembles

To further analyze how the structural ensembles change from the C state to the heated C state and the O state, we applied the principal component analysis (PCA) to the joint C/O-state ensemble (see Materials and Methods section).

The first (second) PCA mode accounts for 22% (14%) of the total conformational variations. To visualize the distributions of the C-state, the heated-C-state, and the O-state ensembles in the conformational space, we projected snapshots of these ensembles onto a two-dimensional plane spanned by the eigenvectors of the first and the second PCA mode (see Fig. 4). The ensembles of the C state and the O state are well separated into two main clusters along the first PCA mode (see Fig. 4),

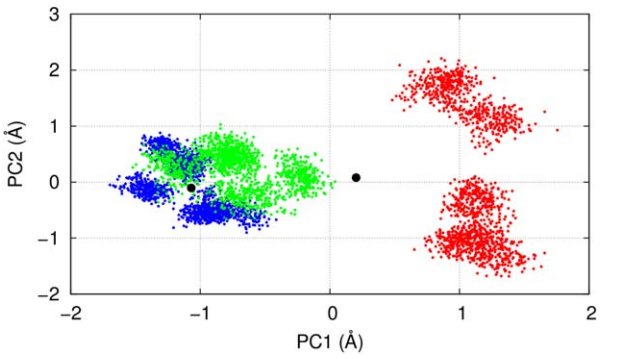

Figure 4

Results of PCA for the joint C/O-state ensembles: projections of the C-state (blue), the heated-C-state (green), and the O-state (red) ensembles onto a plane spanned by the first and the second PCA modes (denoted PC1 and PC2). The two black dots correspond to the closed and open cryo-EM structures of TRPV1. See Supporting Information Movies S1 and S2 for the detailed conformational changes predicted by PC1.

supporting the relevance of this mode to the C-to-O gating transition. The C-state cluster is centered around the closed structure of cryo-EM, while the open structure of cryo-EM is intermediate between the C-state and the O-state cluster (see Fig. 4). This could be attributed to reduced C-to-O conformational changes under the cryo-EM conditions (e.g., due to restraints of detergents around the TMD). Interestingly, the heated-C-state ensemble is shifted away from the C-state cluster toward the O-state cluster by ~0.5 Å along the first PCA mode (see Fig. 4), suggesting that this key mode can be partially activated by heat. Compared with the C-state cluster, the O-state cluster is more widely distributed by separating into two sub-clusters along the second PCA mode. Therefore, the O-state ensemble is structurally more diverse than the C-state ensemble, which is in agreement with our analyses of all-to-all RMSD (see Supporting Information Fig. S2) and RMSF (see Fig. 2).

The first PCA mode describes inward motions of the outer pore, the MPD linkers, and the TRP helices, along with a bending at the junctions between the TRP helices and the S6 helices (see Supporting Information Movies S1 and S2). Additionally, the lower gate at I679 slightly expands, while the upper gate residues G643 move downward (see Supporting Information Movie S2). As expected, the above motions resemble the observed changes between the average structures of the C-state and the O-state ensembles [see Fig. 1(c, d)]. Based on these observations, we propose that upon heat activation the MPD linkers move inward and cause a bending at the S6-TRP helix junctions, thus enabling the lower S6 helices to bulge outward to open the lower gate (see Supporting Information Movie S2). This putative pathway is distinct from a previously proposed vanilloid-activated pathway involving the S2–S3 linker[87] and the S4–S5 linker.[35] Consistent with our proposal, a loose S6-TRP helix coupling in a TRPV2 structure resulted in a non-conductive state.[54]

Distinct hydrogen bonds form in the C/O state and partially form upon heat activation

To probe dynamic interactions underlying the C-to-O conformational changes in TRPV1, we identified a

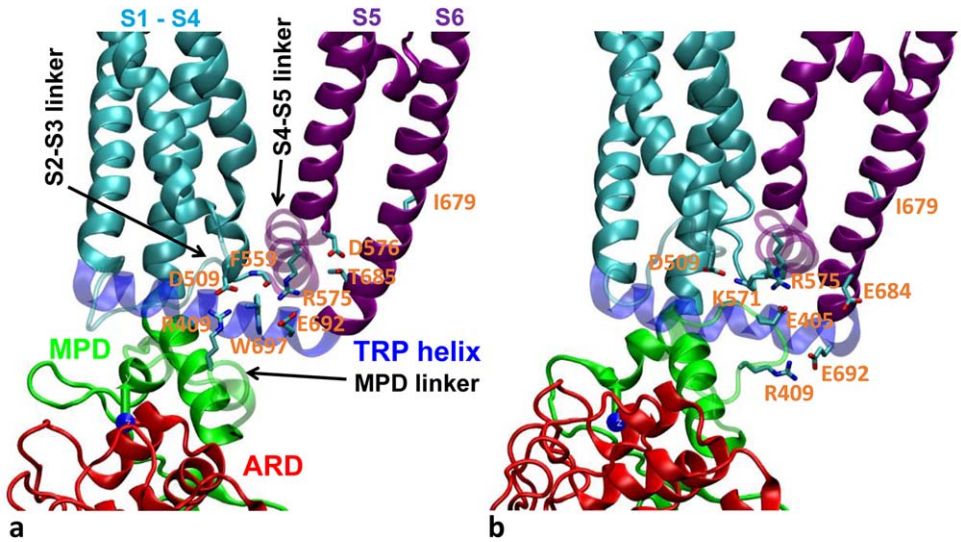

Figure 5

Representative snapshots of HB-forming residue pairs which are specific to (**a**) the C state and (**b**) the O state. For clarity, the MPD linker, the S2–S3 linker, the S4–S5 linker, and the TRP helix are shown as transparent. Sidechains of key HB-forming residues are shown and colored by atom: nitrogen (blue), carbon (cyan), and oxygen (red). Same color coding as Figure 1(a) is used for the various domains. See Table I for further details.

Table I
HB-Forming Residue Pairs and Occupancy in the C State, the Heated C State, and the O State

HB-forming residue pair and occupancy		
C state at 30°C	Heated C state at 60°C	O state at 60°C
GLU327 LYS392 0.42[a]	**LYS318 GLU359** 0.33[a]	**LYS318 GLU359** 0.36[a]
ARG355 ARG367 0.91	**GLU326 ARG367** 0.43	**GLU326 ARG367** 1.46
ARG355 LYS368 0.37	ILE352 ARG367 0.33	**GLU327 ARG367** 0.95
GLU356 LYS368 0.75	**ARG355 LEU365** 0.87	**ARG355 LEU365** 0.99
GLU356 THR370 0.34	ARG355 ARG367 0.91	ARG355 ARG367 0.70
ILE357 SER366 0.78	ARG355 LYS368 0.41	ARG355 LYS368 0.44
GLU397 LYS710 0.64	GLU356 LYS368 0.72	GLU356 LYS368 0.62
ARG409 ASP509 1.10	GLU356 THR370 0.78	GLU356 THR370 0.32
GLN423 ARG701 0.56	ILE357 SER366 0.84	ILE357 SER366 0.55
LYS425 GLU709 1.01	GLU397 LYS710 0.55	**GLU397 ARG499** 0.45
ARG499 ASP707 0.58	*ARG409 ASP509* 0.78	GLU397 LYS710 0.86
SER510 GLU570 0.41	**ARG409 GLU692** 0.31	**GLU405 ARG575** 0.76
TYR511 GLU570 0.38	GLN423 ARG701 0.80	**ARG409 GLU692** 1.49
SER512 GLU570 0.55	LYS425 GLU709 0.58	GLN423 ARG701 0.59
PHE559 TRP697 0.41	ARG499 ASP707 0.92	LYS425 GLU709 0.55
ARG575 GLU692 1.63	SER510 GLU570 0.82	ARG499 ASP707 0.83
ASP576 THR685 0.38	TYR511 GLU570 0.51	**ASP509 LYS571** 0.64
TYR584 THR641 0.62	SER512 GLU570 1.14	**ASP509 ARG575** 0.62
TYR584 TYR666 0.40	*PHE559 TRP697* 0.46	SER510 GLU570 0.72
LEU637 TYR666 0.58	*ARG575 GLU692* 1.73	TYR511 GLU570 0.51
THR641 TYR666 0.49	*ASP576 THR685* 0.41	SER512 GLU570 0.73
	TYR584 THR641 0.76	**ARG575 GLU684** 0.39
	TYR584 TYR666 0.38	TYR584 THR641 0.75
	LEU637 TYR666 0.66	TYR584 TYR666 0.31
	THR641 TYR666 0.46	LEU637 TYR666 0.34
	THR641 THR670 0.30	**THR641 THR670** 0.56

[a]The C-state and O-state specific HB-forming residue pairs are in italic and bold font, respectively.

network of hydrogen bonds (HB) specific to the C state or the O state (with occupancy $\geq$0.3, see Materials and Methods section). We focus on those HBs that couple between key domains of TRPV1 (including the ARD, the MPD, the S2–S3 linker, the S4–S5 linker, the S5 helix, the outer pore, the S6 helix, and the TRP helix, see Fig. 5).

We found the following C-state-specific HB-forming residue pairs (i.e., with HB forming in the C state at 30°C but not in the O state at 60°C, see Table I and Fig. 5): (E327, K392), (R409, D509), (F559, W697), (R575, E692), (D576, T685), and (T641, Y666). Similarly, we identified the following O-state-specific HB-forming residue pairs (see Table I and Fig. 5): (K318, E359), (E326, R367), (E327, R367), (R355, L365), (E397, R499), (E405, R575), (R409, E692), (D509, K571), (D509, R575), (R575, E684), and (T641, T670). In the heated-C-state ensemble, we observed a mixture of C/O-state-specific HBs (see Table I), and most O-state-specific HBs are partially formed with intermediate occupancy (see Table II). In particular, the O-state-specific HB between R409 of the MPD linker and E692 of the TRP helix forms partially in the heated C state, which is associated with the heat-activated motions of the MPD linker and the TRP helix [see Fig. 1(c,d)].

Table II
State-Dependent Occupancy for the HB-Forming Residue Pairs Specific to the O State

O-state-specific HB-forming residue pair and occupancy			
Residue pair	C state at 30°C	Heated C state at 60°C	O state at 60°C
LYS318 GLU359	0.17	0.33	0.36
GLU326 ARG367	0.06	0.43	1.46
GLU327 ARG367	0.02	0.20	0.95
ARG355 LEU365	0.10	0.87	0.99
GLU397 ARG499	0.00	0.19	0.45
GLU405 ARG575	0.00	0.02	0.76
ARG409 GLU692	0.05	0.31	1.49
ASP509 LYS571	0.20	0.26	0.64
ASP509 ARG575	0.02	0.05	0.62
ARG575 GLU684	0.00	0.17	0.39
THR641 THR670	0.10	0.30	0.56

Taken together, the above HB interactions dynamically couple the ARD (K318, E326, E327, and R355), the MPD (E359, L365, R367, K392, E397, E405, and R409), the S2–S3 linker (R499 and D509), the S4–S5 linker (F559, K571, R575, and D576), the outer pore (T641), the S6 helix (Y666, T670, E684, and T685), and the TRP helix (E692 and W697), which may underlie the putative heat-evoked pathway from the ARD/MPD to the lower gate via the TRP helix, the S2–S3 linker, and the S4–S5 linker. In support of this proposal, our previous MD simulation found R409 among the three top-contributing residues to the C-to-O van der Waals energy difference (T406, R409, and M412).[66] Some of the above key residues can be validated by previous mutational studies. The mutations of R575,[96] E692,[97] and W697[98,99] were found to impair TRPV1's responses to various stimuli.[100] The T406D mutation caused higher heat sensitivity,[101] supporting the role of T406 (and the neighboring E405) in stabilizing the O state. K571 is involved in voltage sensing and in TRPV1-lipid/ligand interactions.[100] D576 is involved in voltage/capsaicin-dependent gating of TRPV1.[100] The mutations in T641 and E684 resulted in gain-of-function TRPV1 variants.[89] Future mutational studies of those HB-forming residues will validate their roles in tuning the C-to-O thermodynamic equilibrium of TRPV1 gating.

DISCUSSION AND CONCLUSION

Our MD simulations of the C state at 30°C revealed a stably closed channel constricted at the lower gate (near residue I679), while the upper gate (near residues G643 and M644) is more dynamic and undergoes transient opening/closing [see Fig. 3(a)]. This finding is consistent with our previous coarse-grained modeling of TRPV1 which found G643 is more flexible than I679, and therefore the upper gate may open more readily than the lower gate during the gating transition.[66] Our MD simulations of the O state at 60°C showed that the channel pore is dynamic at both the lower and the upper gate [see Fig. 3(b)]. The O

state exhibits greater structural variation than the C state, which is consistent with a higher entropy in the O state required for the heat activation. Specifically, we observed pronounced C-to-O increases in flexibility in key regions including the MPD linker, the S5 helix, the S6 helix, and the TRP helix (see Fig. 2). Some of these regions (including the MPD linker and the lower S6 helix) also exhibit heat-activated flexibility increases in the C state (see Fig. 2). By comparing the ensemble-averaged structures and the first PCA mode, we found large gating-related motions in the outer pore, the MPD linker, and the TRP helix [see Fig. 1(c,d), Supporting Information Movies S1 and S2], and the forming/breaking of the O/C-state specific HBs (see Fig. 5). Interestingly, these motions and the O-state-specific HBs were partially observed in the heated C-state ensemble, suggesting that they are likely involved in the heat activation of TRPV1. We note the first PCA mode reveals similar large motions of key domains (see Supporting Information Movies S1 and S2) as found in our previous coarse-grained transition pathway modeling,[66] although these domain motions are highly concerted and do not exhibit any motional sequence as observed in our coarse-grained modeling.[66]

Despite our encouraging observations of those fast heat-activated changes in dynamics and interactions, we did not observe a complete gating transition within the 200-ns simulation time. In future studies, more extensive MD simulation and its accelerated[102] or targeted[103] variants will be performed to directly observe the heat-activated gating transition in TRPV1 and analyze its kinetic behaviors. We are in the process of conducting more MD simulations using the newly solved higher resolution structure of TRPV1.[52] Preliminary analysis revealed very similar dynamic behaviors (e.g., flexible CTD, dynamic upper gate, etc.) as observed in the MD simulations of the old structure.[51] Detailed results will be reported in a future publication.

ACKNOWLEDGMENTS

W.Z. thanks Dr. Alan Grossfield for useful discussion of MD simulation. Computational support was provided by the Center for Computational Research at the University at Buffalo and the Biowulf system at the National Institutes of Health. The authors declare no competing financial interests.

REFERENCES

1. Clapham DE. TRP channels as cellular sensors. Nature 2003;426:517–524.
2. Voets T, Talavera K, Owsianik G, Nilius B. Sensing with TRP channels. Nat Chem Biol 2005;1:85–92.
3. Caterina MJ, Rosen TA, Tominaga M, Brake AJ, Julius D. A capsaicin-receptor homologue with a high threshold for noxious heat. Nature 1999;398:436–441.
4. Caterina MJ, Schumacher MA, Tominaga M, Rosen TA, Levine JD, Julius D. The capsaicin receptor: a heat-activated ion channel in the pain pathway. Nature 1997;389:816–824.
5. Story GM, Peier AM, Reeve AJ, Eid SR, Mosbacher J, Hricik TR, Earley TJ, Hergarden AC, Andersson DA, Hwang SW, McIntyre P, Jegla T, Bevan S, Patapoutian A. ANKTM1, a TRP-like channel expressed in nociceptive neurons, is activated by cold temperatures. Cell 2003;112:819–829.
6. Nilius B, Appendino G, Owsianik G. The transient receptor potential channel TRPA1: from gene to pathophysiology. Pflugers Arch 2012;464:425–458.
7. Karashima Y, Talavera K, Everaerts W, Janssens A, Kwan KY, Vennekens R, Nilius B, Voets T. TRPA1 acts as a cold sensor in vitro and in vivo. Proc Natl Acad Sci USA 2009;106:1273–1278.
8. Voets T, Droogmans G, Wissenbach U, Janssens A, Flockerzi V, Nilius B. The principle of temperature-dependent gating in cold- and heat-sensitive TRP channels. Nature 2004;430:748–754.
9. Jordt SE, Tominaga M, Julius D. Acid potentiation of the capsaicin receptor determined by a key extracellular site. Proc Natl Acad Sci USA 2000;97:8134–8139.
10. Tominaga M, Caterina MJ, Malmberg AB, Rosen TA, Gilbert H, Skinner K, Raumann BE, Basbaum AI, Julius D. The cloned capsaicin receptor integrates multiple pain-producing stimuli. Neuron 1998;21:531–543.
11. Howard J, Bechstedt S. Hypothesis: a helix of ankyrin repeats of the NOMPC-TRP ion channel is the gating spring of mechanoreceptors. Curr Biol 2004;14:R224–R226.
12. Sotomayor M, Corey DP, Schulten K. In search of the hair-cell gating spring elastic properties of ankyrin and cadherin repeats. Structure 2005;13:669–682.
13. Yin J, Kuebler WM. Mechanotransduction by TRP channels: general concepts and specific role in the vasculature. Cell Biochem Biophys 2010;56:1–18.
14. Gunthorpe MJ, Szallasi A. Peripheral TRPV1 receptors as targets for drug development: new molecules and mechanisms. Curr Pharm Des 2008;14:32–41.
15. Nilius B. Transient receptor potential TRP channels as therapeutic drug targets: next round! Curr Top Med Chem 2013;13:244–246.
16. Nilius B, Voets T, Peters J. TRP channels in disease. Sci STKE 2005;2005:re8.
17. Nilius B. TRP channels in disease. Biochim Biophys Acta 2007;1772:805–812.
18. Catterall WA. Ion channel voltage sensors: structure, function, and pathophysiology. Neuron 2010;67:915–928.
19. Catterall WA. Voltage-gated sodium channels at 60: structure, function and pathophysiology. J Physiol 2012;590:2577–2589.
20. Baez D, Raddatz N, Ferreira G, Gonzalez C, Latorre R. Gating of thermally activated channels. Curr Top Membr 2014;74:51–87.
21. Gaudet R. A primer on ankyrin repeat function in TRP channels and beyond. Mol Biosyst 2008;4:372–379.
22. Montell C. Physiology, phylogeny, and functions of the TRP superfamily of cation channels. Sci STKE 2001;2001:re1.
23. Garcia-Sanz N, Valente P, Gomis A, Fernandez-Carvajal A, Fernandez-Ballester G, Viana F, Belmonte C, Ferrer-Montiel A. A role of the transient receptor potential domain of vanilloid receptor I in channel gating. J Neurosci 2007;27:11641–11650.
24. Numazaki M, Tominaga T, Takeuchi K, Murayama N, Toyooka H, Tominaga M. Structural determinant of TRPV1 desensitization interacts with calmodulin. Proc Natl Acad Sci USA 2003;100:8002–8006.
25. Prescott ED, Julius D. A modular PIP2 binding site as a determinant of capsaicin receptor sensitivity. Science 2003;300:1284–1288.
26. Yao J, Liu B, Qin F. Modular thermal sensors in temperature-gated transient receptor potential (TRP) channels. Proc Natl Acad Sci USA 2011;108:11109–11114.
27. Brauchi S, Orta G, Mascayano C, Salazar M, Raddatz N, Urbina H, Rosenmann E, Gonzalez-Nilo F, Latorre R. Dissection of the

components for PIP2 activation and thermosensation in TRP channels. Proc Natl Acad Sci USA 2007;104:10246–10251.
28. Brauchi S, Orta G, Salazar M, Rosenmann E, Latorre R. A hot-sensing cold receptor: C-terminal domain determines thermosensation in transient receptor potential channels. J Neurosci 2006;26: 4835–4840.
29. Vlachova V, Teisinger J, Susankova K, Lyfenko A, Ettrich R, Vyklicky L. Functional role of C-terminal cytoplasmic tail of rat vanilloid receptor 1. J Neurosci 2003;23:1340–1350.
30. Cui Y, Yang F, Cao X, Yarov-Yarovoy V, Wang K, Zheng J. Selective disruption of high sensitivity heat activation but not capsaicin activation of TRPV1 channels by pore turret mutations. J Gen Physiol 2012;139:273–283.
31. Yang F, Cui Y, Wang K, Zheng J. Thermosensitive TRP channel pore turret is part of the temperature activation pathway. Proc Natl Acad Sci USA 2010;107:7083–7088.
32. Kim SE, Patapoutian A, Grandl J. Single residues in the outer pore of TRPV1 and TRPV3 have temperature-dependent conformations. PLoS One 2013;8:e59593.
33. Grandl J, Kim SE, Uzzell V, Bursulaya B, Petrus M, Bandell M, Patapoutian A. Temperature-induced opening of TRPV1 ion channel is stabilized by the pore domain. Nat Neurosci 2010;13:708–714.
34. Latorre R, Brauchi S, Orta G, Zaelzer C, Vargas G. ThermoTRP channels as modular proteins with allosteric gating. Cell Calcium 2007;42:427–438.
35. Cao E, Liao M, Cheng Y, Julius D. TRPV1 structures in distinct conformations reveal activation mechanisms. Nature 2013;504: 113–118.
36. Bagneris C, Naylor CE, McCusker EC, Wallace BA. Structural model of the open-closed-inactivated cycle of prokaryotic voltage-gated sodium channels. J Gen Physiol 2015;145:5–16.
37. Cvetkov TL, Huynh KW, Cohen MR, Moiseenkova-Bell VY. Molecular architecture and subunit organization of TRPA1 ion channel revealed by electron microscopy. J Biol Chem 2011;286:38168–38176.
38. Huynh KW, Cohen MR, Chakrapani S, Holdaway HA, Stewart PL, Moiseenkova-Bell VY. Structural insight into the assembly of TRPV channels. Structure 2014;22:260–268.
39. Maruyama Y, Ogura T, Mio K, Kiyonaka S, Kato K, Mori Y, Sato C. Three-dimensional reconstruction using transmission electron microscopy reveals a swollen, bell-shaped structure of transient receptor potential melastatin type 2 cation channel. J Biol Chem 2007;282:36961–36970.
40. Mio K, Ogura T, Hara Y, Mori Y, Sato C. The non-selective cation-permeable channel TRPC3 is a tetrahedron with a cap on the large cytoplasmic end. Biochem Biophys Res Commun 2005;333:768–777.
41. Mio K, Ogura T, Kiyonaka S, Hiroaki Y, Tanimura Y, Fujiyoshi Y, Mori Y, Sato C. The TRPC3 channel has a large internal chamber surrounded by signal sensing antennas. J Mol Biol 2007;367: 373–383.
42. Moiseenkova-Bell VY, Stanciu LA, Serysheva II, Tobe BJ, Wensel TG. Structure of TRPV1 channel revealed by electron cryomicroscopy. Proc Natl Acad Sci USA 2008;105:7451–7455.
43. Shigematsu H, Sokabe T, Danev R, Tominaga M, Nagayama K. A 3.5-nm structure of rat TRPV4 cation channel revealed by Zernike phase-contrast cryoelectron microscopy. J Biol Chem 2010;285: 11210–11218.
44. Inada H, Procko E, Sotomayor M, Gaudet R. Structural and biochemical consequences of disease-causing mutations in the ankyrin repeat domain of the human TRPV4 channel. Biochemistry 2012; 51:6195–6206.
45. Jin X, Touhey J, Gaudet R. Structure of the N-terminal ankyrin repeat domain of the TRPV2 ion channel. J Biol Chem 2006;281: 25006–25010.
46. Lishko PV, Procko E, Jin X, Phelps CB, Gaudet R. The ankyrin repeats of TRPV1 bind multiple ligands and modulate channel sensitivity. Neuron 2007;54:905–918.
47. McCleverty CJ, Koesema E, Patapoutian A, Lesley SA, Kreusch A. Crystal structure of the human TRPV2 channel ankyrin repeat domain. Protein Sci 2006;15:2201–2206.
48. Phelps CB, Huang RJ, Lishko PV, Wang RR, Gaudet R. Structural analyses of the ankyrin repeat domain of TRPV6 and related TRPV ion channels. Biochemistry 2008;47:2476–2484.
49. Shi DJ, Ye S, Cao X, Zhang R, Wang K. Crystal structure of the N-terminal ankyrin repeat domain of TRPV3 reveals unique conformation of finger 3 loop critical for channel function. Protein Cell 2013;4:942–950.
50. Landoure G, Zdebik AA, Martinez TL, Burnett BG, Stanescu HC, Inada H, Shi Y, Taye AA, Kong L, Munns CH, Choo SS, Phelps CB, Paudel R, Houlden H, Ludlow CL, Caterina MJ, Gaudet R, Kleta R, Fischbeck KH, Sumner CJ. Mutations in TRPV4 cause Charcot-Marie-Tooth disease type 2C. Nat Genet 2010;42:170–174.
51. Liao M, Cao E, Julius D, Cheng Y. Structure of the TRPV1 ion channel determined by electron cryo-microscopy. Nature 2013;504: 107–112.
52. Gao Y, Cao E, Julius D, Cheng Y. TRPV1 structures in nanodiscs reveal mechanisms of ligand and lipid action. Nature 2016;534: 347–351.
53. Huynh KW, Cohen MR, Jiang J, Samanta A, Lodowski DT, Zhou ZH, Moiseenkova-Bell VY. Structure of the full-length TRPV2 channel by cryo-EM. Nat Commun 2016;7:11130.
54. Zubcevic L, Herzik MA, Jr., Chung BC, Liu Z, Lander GC, Lee SY. Cryo-electron microscopy structure of the TRPV2 ion channel. Nat Struct Mol Biol 2016;23:180–186.
55. Karplus M, McCammon JA. Molecular dynamics simulations of biomolecules. Nat Struct Biol 2002;9:646–652.
56. Nury H, Poitevin F, Van Renterghem C, Changeux JP, Corringer PJ, Delarue M, Baaden M. One-microsecond molecular dynamics simulation of channel gating in a nicotinic receptor homologue. Proc Natl Acad Sci USA 2010;107:6275–6280.
57. Nury H, Van Renterghem C, Weng Y, Tran A, Baaden M, Dufresne V, Changeux JP, Sonner JM, Delarue M, Corringer PJ. X-ray structures of general anaesthetics bound to a pentameric ligand-gated ion channel. Nature 2011;469:428–431.
58. Zhu F, Hummer G. Pore opening and closing of a pentameric ligand-gated ion channel. Proc Natl Acad Sci USA 2010;107:19814–19819.
59. Jensen MO, Jogini V, Borhani DW, Leffler AE, Dror RO, Shaw DE. Mechanism of voltage gating in potassium channels. Science 2012; 336:229–233.
60. Stone JE, Hardy DJ, Ufimtsev IS, Schulten K. GPU-accelerated molecular modeling coming of age. J Mol Graph Model 2010;29: 116–125.
61. Atilgan AR, Durell SR, Jernigan RL, Demirel MC, Keskin O, Bahar I. Anisotropy of fluctuation dynamics of proteins with an elastic network model. Biophys J 2001;80:505–515.
62. Tama F, Sanejouand YH. Conformational change of proteins arising from normal mode calculations. Protein Eng 2001;14:1–6.
63. Zheng W, Doniach S. A comparative study of motor-protein motions by using a simple elastic-network model. Proc Natl Acad Sci USA 2003;100:13253–13258.
64. Tozzini V. Coarse-grained models for proteins. Curr Opin Struct Biol 2005;15:144–150.
65. Tozzini V. Minimalist models for proteins: a comparative analysis. Q Rev Biophys 2010;43:333–371.
66. Zheng W, Qin F. A combined coarse-grained and all-atom simulation of TRPV1 channel gating and heat activation. J Gen Physiol 2015;145:443–456.
67. Lomize MA, Lomize AL, Pogozheva ID, Mosberg HI. OPM: orientations of proteins in membranes database. Bioinformatics 2006;22: 623–625.
68. Fiser A, Sali A. ModLoop: automated modeling of loops in protein structures. Bioinformatics 2003;19:2500–2501.

69. Jo S, Kim T, Im W. Automated builder and database of protein/membrane complexes for molecular dynamics simulations. PLoS One 2007;2:
70. Wu EL, Cheng X, Jo S, Rui H, Song KC, Davila-Contreras EM, Qi Y, Lee J, Monje-Galvan V, Venable RM, Klauda JB, Im W. CHARMM-GUI membrane builder toward realistic biological membrane simulations. J Comput Chem 2014;35:1997–2004.
71. Jo S, Lim JB, Klauda JB, Im W. CHARMM-GUI membrane builder for mixed bilayers and its application to yeast membranes. Biophys J 2009;97:50–58.
72. Jo S, Kim T, Iyer VG, Im W. CHARMM-GUI: a web-based graphical user interface for CHARMM. J Comput Chem 2008;29:1859–1865.
73. Lee J, Cheng X, Swails JM, Yeom MS, Eastman PK, Lemkul JA, Wei S, Buckner J, Jeong JC, Qi Y, Jo S, Pande VS, Case DA, Brooks CL, 3rd, MacKerell AD, Jr., Klauda JB, Im W. CHARMM-GUI Input Generator for NAMD, GROMACS, AMBER, OpenMM, and CHARMM/OpenMM Simulations Using the CHARMM36 Additive Force Field. J Chem Theory Comput 2016;12:405–413.
74. Martyna GJ, Hughes A, Tuckerman ME. Molecular dynamics algorithms for path integrals at constant pressure. J Chem Phys 1999; 110:3275–3290.
75. Parrinello M, Rahman A. Polymorphic transitions in single crystals: a new molecular dynamics method. J Appl Phys 1981;52:7182–7190.
76. Darden T, York D, Pedersen L. Particle mesh Ewald: an N·log(N) method for Ewald sums in large systems. J Chem Phys 1993;98: 10089–10092.
77. Hess B, Bekker H, Berendsen HJC, Fraaije JGEM. LINCS: a linear constraint solver for molecular simulations. J Comput Chem 1997; 18:1463–1472.
78. Pronk S, Pall S, Schulz R, Larsson P, Bjelkmar P, Apostolov R, Shirts MR, Smith JC, Kasson PM, van der Spoel D, Hess B, Lindahl E. GROMACS 4.5: a high-throughput and highly parallel open source molecular simulation toolkit. Bioinformatics 2013;29: 845–854.
79. Huang J, MacKerell AD, Jr. CHARMM36 all-atom additive protein force field: validation based on comparison to NMR data. J Comput Chem 2013;34:2135–2145.
80. Klauda JB, Venable RM, Freites JA, O'Connor JW, Tobias DJ, Mondragon-Ramirez C, Vorobyov I, MacKerell AD, Jr, Pastor RW. Update of the CHARMM all-atom additive force field for lipids: validation on six lipid types. J Phys Chem B 2010;114:7830–7843.
81. Jorgensen WL, Chandrasekhar J, Madura JD, Impey RW, Klein ML. Comparison of simple potential functions for simulating liquid water. J Chem Phys 1983;79:926–935.
82. Humphrey W, Dalke A, Schulten K. VMD: visual molecular dynamics. J Mol Graph 1996;14:33–38.
83. Yao J, Liu B, Qin F. Kinetic and energetic analysis of thermally activated TRPV1 channels. Biophys J 2010;99:1743–1753.
84. Shrivastava IH, Sansom MS. Simulations of ion permeation through a potassium channel: molecular dynamics of KcsA in a phospholipid bilayer. Biophys J 2000;78:557–570.
85. Kulleperuma K, Smith SM, Morgan D, Musset B, Holyoake J, Chakrabarti N, Cherny VV, DeCoursey TE, Pomes R. Construction and validation of a homology model of the human voltage-gated proton channel hHV1. J Gen Physiol 2013;141:445–465.
86. Jogini V, Roux B. Dynamics of the Kv1.2 voltage-gated K+ channel in a membrane environment. Biophys J 2007;93:3070–3082.
87. Jordt SE, Julius D. Molecular basis for species-specific sensitivity to "hot" chili peppers. Cell 2002;108:421–430.
88. Ryu S, Liu B, Yao J, Fu Q, Qin F. Uncoupling proton activation of vanilloid receptor TRPV1. J Neurosci 2007;27:12797–12807.
89. Myers BR, Bohlen CJ, Julius D. A yeast genetic screen reveals a critical role for the pore helix domain in TRP channel gating. Neuron 2008;58:362–373.
90. Welch JM, Simon SA, Reinhart PH. The activation mechanism of rat vanilloid receptor 1 by capsaicin involves the pore domain and differs from the activation by either acid or heat. Proc Natl Acad Sci USA 2000;97:13889–13894.
91. Smart OS, Neduvelil JG, Wang X, Wallace BA, Sansom MS. HOLE: a program for the analysis of the pore dimensions of ion channel structural models. J Mol Graph 1996;14:354–360.
92. Salazar H, Jara-Oseguera A, Hernandez-Garcia E, Llorente I, Arias O, II, Soriano-Garcia M, Islas LD, Rosenbaum T. Structural determinants of gating in the TRPV1 channel. Nat Struct Mol Biol 2009; 16:704–710.
93. Hui K, Liu B, Qin F. Capsaicin activation of the pain receptor, VR1: multiple open states from both partial and full binding. Biophys J 2003;84:2957–2968.
94. Liu B, Hui K, Qin F. Thermodynamics of heat activation of single capsaicin ion channels VR1. Biophys J 2003;85:2988–3006.
95. Wang S, Vafabakhsh R, Borschel WF, Ha T, Nichols CG. Structural dynamics of potassium-channel gating revealed by single-molecule FRET. Nat Struct Mol Biol 2016;23:31–36.
96. Voets T, Owsianik G, Janssens A, Talavera K, Nilius B. TRPM8 voltage sensor mutants reveal a mechanism for integrating thermal and chemical stimuli. Nat Chem Biol 2007;3:174–182.
97. Gregorio-Teruel L, Valente P, Liu B, Fernandez-Ballester G, Qin F, Ferrer-Montiel A. The integrity of the TRP domain is pivotal for correct TRPV1 channel gating. Biophys J 2015;109:529–541.
98. Valente P, Garcia-Sanz N, Gomis A, Fernandez-Carvajal A, Fernandez-Ballester G, Viana F, Belmonte C, Ferrer-Montiel A. Identification of molecular determinants of channel gating in the transient receptor potential box of vanilloid receptor I. FASEB J 2008;22:3298–3309.
99. Gregorio-Teruel L, Valente P, Gonzalez-Ros JM, Fernandez-Ballester G, Ferrer-Montiel A. Mutation of I696 and W697 in the TRP box of vanilloid receptor subtype I modulates allosteric channel activation. J Gen Physiol 2014;143:361–375.
100. Winter Z, Buhala A, Otvos F, Josvay K, Vizler C, Dombi G, Szakonyi G, Olah Z. Functionally important amino acid residues in the transient receptor potential vanilloid 1 (TRPV1) ion channel–an overview of the current mutational data. Mol Pain 2013;9:30.
101. Jendryke T, Prochazkova M, Hall BE, Nordmann GC, Schladt M, Milenkovic VM, Kulkarni AB, Wetzel CH. TRPV1 function is modulated by Cdk5-mediated phosphorylation: insights into the molecular mechanism of nociception. Sci Rep 2016;6:22007.
102. Hamelberg D, Mongan J, McCammon JA. Accelerated molecular dynamics: a promising and efficient simulation method for biomolecules. J Chem Phys 2004;120:11919–11929.
103. Schlitter J, Engels M, Kruger P. Targeted molecular dynamics: a new approach for searching pathways of conformational transitions. J Mol Graph 1994;12:84–89.